



Full Text View

[Volume 29, Issue 12 \(December 1999\)](#)

Journal of Physical Oceanography

Article: pp. 3056–3072 | [Abstract](#) | [PDF \(421K\)](#)

Near-Bottom Turbulence Measurements in a Partially Mixed Estuary: Turbulent Energy Balance, Velocity Structure, and Along-Channel Momentum Balance

J. H. Trowbridge, W. R. Geyer, M. M. Bowen, and A. J. Williams III

Woods Hole Oceanographic Institution, Woods Hole, Massachusetts

(Manuscript received May 6, 1998, in final form February 1, 1999)

DOI: 10.1175/1520-0485(1999)029<3056:NBTMIA>2.0.CO;2

ABSTRACT

A set of moored, bottom-mounted and shipboard measurements, obtained in a straight section of the lower Hudson estuary during late summer and early fall of 1995, determine velocity, density, and along-channel pressure gradient throughout the 15-m water column, as well as providing direct eddy-correlation estimates of Reynolds stress and indirect inertial-range estimates of dissipation within 3 m of the bottom. The analysis focuses on testing 1) a simplified turbulent kinetic energy equation, in which production balances dissipation; 2) the Prandtl–Karman law of the wall, which is a relationship between bottom stress and near-bottom velocity gradient; and 3) a simplified depth-integrated along-channel momentum balance involving local acceleration, pressure gradient, and bottom stress. Estimates of production and dissipation agree well throughout the entire record. The relationship between bottom stress and velocity gradient is consistent with the law of the wall within approximately 1 m of the seafloor during flooding tides, but it departs from the law of the wall at greater heights during flooding tides and at all resolved heights during ebbing tides. The local stratification is too small to explain this effect, and the likely explanation is suppression of the turbulent length scale by the finite thickness of the relatively well-mixed layer beneath the pycnocline. Direct covariance estimates of bottom stress close the approximate momentum balance well during some periods, but are often smaller than the sum of the other terms in the balance by a factor of roughly up to 2. The agreement between stress estimates and the sum of the other terms is best during periods of strongest top-to-bottom stratification and worst during periods of weak stratification, for reasons that are not understood.

Table of Contents:

- [Introduction](#)
- [Methods](#)
- [Results](#)
- [Discussion](#)
- [Summary and conclusions](#)
- [REFERENCES](#)
- [FIGURES](#)

Options:

- [Create Reference](#)
- [Email this Article](#)
- [Add to MyArchive](#)
- [Search AMS Glossary](#)

Search CrossRef for:

- [Articles Citing This Article](#)

Search Google Scholar for:

- [J. H. Trowbridge](#)
- [W. R. Geyer](#)
- [M. M. Bowen](#)
- [A. J. Williams](#)

1. Introduction

Researchers working in the coastal ocean have reported near-bottom measurements of turbulence for decades. Analyses of these measurements have focused on a number of questions including estimation of integral scales ([Bowden and Fairburn 1952, 1956](#); [Bowden 1962](#)), the relationship between turbulent shear stress and turbulence intensity ([Gordon and Dohne 1973](#); [Gross and Nowell 1983](#); [Gross et al. 1986](#)), the statistics and intermittency of the instantaneous Reynolds stress and the occurrence of bursts and sweeps ([Gordon 1974](#); [Heathershaw 1974, 1979](#); [Heathershaw and Simpson 1978](#)), spectral scaling laws ([Soulsby 1977](#); [Heathershaw 1979](#); [Gross and Nowell 1985](#)), the use of indirect inertial-range techniques to estimate Reynolds stress ([Huntley 1988](#); [Green 1992](#); [Gross et al. 1994](#)), and variability of the bottom drag coefficient due to form drag ([McLean and Smith 1979](#)), wave–current interaction ([Grant et al. 1984](#); [Huntley and Hazen 1988](#)), and stratification by suspended sediment ([Green and McCave 1995](#)).

In spite of the substantial previous work, a set of fundamental issues related to near-bottom turbulence characteristics in the coastal ocean has received little or no attention. In particular, no one has reported, with direct measurements of the quantities involved, an observational test of the lowest-order horizontal momentum equation that has traditionally been assumed to hold in shallow water, where frictional effects are important. In addition, only one study ([Gross and Nowell 1985](#)) has tested the simplified turbulent energy balance (production equals dissipation) that is typically assumed to hold near a solid boundary, and only a few studies ([Smith and McLean 1977](#); [Soulsby and Dyer 1981](#)) have attempted systematic explanations of observed departures of the Reynolds-averaged velocity profile from the Prandtl–Karman law of the wall.

During late summer and early fall of 1995, we undertook a study of estuarine dynamics in a straight section of the lower Hudson estuary. In this study, a set of moored and tripod-mounted instrumentation obtained time series of velocity and salinity throughout the water column at a central site, together with measurements of turbulent Reynolds stress and turbulence dissipation near the seafloor. Other tripod-mounted instrumentation obtained time series of bottom pressure and salinity at several secondary sites, and periodic shipboard surveys resolved the tidal variability and vertical structure of velocity and salinity along a set of along-channel and cross-channel transects.

Here we report a subset of the measurements and analysis, focusing on a comparison of observations and simple theory, as expressed by three equations. The first two equations involve the local dynamics of the near-bottom turbulence, and the third equation relates the near-bottom turbulence characteristics to the estuary-wide dynamics. The first equation is an approximation to the turbulent kinetic energy balance (e.g., [Tennekes and Lumley 1972](#)) in which production is equal to dissipation:

$$-\overline{u'w'} \frac{\partial u}{\partial z} = \epsilon. \quad (1)$$

The second equation is the semiempirical Prandtl–Karman law of the wall, which relates the near-bottom velocity field to the bottom shear stress (e.g., [Schlichting 1979](#)):

$$\kappa z \frac{\partial u}{\partial z} = |\tau_b / \rho_0|^{1/2} \text{sgn}(\tau_b). \quad (2)$$

The third equation is an approximation to the along-channel momentum balance (e.g., [Phillips 1980](#)), in depth-integrated form:

$$\int_0^h \left(\rho_0 \frac{\partial u}{\partial t} + \frac{\partial p}{\partial x} \right) dz = -\tau_b. \quad (3)$$

Here x is the along-channel coordinate (positive in the direction of the flooding tide), y is the cross-channel coordinate, z is the vertical coordinate (positive upward and equal to zero at the bottom), and t is time. The quantity ρ_0 is a fixed reference density, h is water depth, (u, v, w) is the Reynolds-averaged velocity vector, p is Reynolds-averaged pressure, $\tau = -\rho_0 \overline{u'w'}$ is Reynolds shear stress (where u' and w' are respectively the along-channel and vertical components of the turbulent velocity vector and an overbar denotes a Reynolds average), ϵ is dissipation rate, κ (approximately equal to 0.40) is the empirical von Kármán constant, and τ_b is bottom shear stress.

Although [\(1\)–\(3\)](#) are simple, comparisons of these relationships with observations are important. Scaling arguments and measurements in the laboratory and atmosphere indicate that [\(1\)](#) is approximately correct under unstratified conditions near a flat solid boundary. Under simple conditions, then, [\(1\)](#) provides a means of testing measurements of stress, shear, and dissipation. Under more complex conditions, discrepancies in [\(1\)](#) might determine the importance of other effects, such as

buoyancy and advection. The law of the wall (2) has often been used in oceanography and other disciplines, both in models and as a means of estimating bottom stress from measurements of horizontal velocity. In the ocean, this relationship has rarely been tested, and the limits of its applicability are not well known. Finally, most simple models are based on the assumption that (3) represents the dominant balance in the along-channel momentum equation, at least at tidal timescales, for rectilinear flows in estuaries with simple geometries. However, transverse secondary flows and variable topography have the potential to make momentum fluxes not represented in (3) of primary importance, and it is important to understand the limits of the simple balance.

In the following, we describe measurements and analysis (section 2) leading to an observational evaluation of (1)–(3). We then present and discuss the results (sections 3 and 4) and summarize conclusions (section 5).

2. Methods

a. Measurements

The measurements, described in detail by Fredericks et al. (1998), took place in a section of the lower Hudson estuary (Fig. 1) where the channel is relatively straight and prismatic. The focus of the study was on the region spanned by the central site C and secondary sites B and D, each of which was in the thalweg of the channel. Measurements at secondary sites E and F, in shallower water near the western bank, provided information about cross-channel variability, and measurements at secondary site A, near the southern tip of Manhattan, provided information about variability produced by the inflow from New York Harbor. The thalweg depths at sites B, C, and D are approximately 17, 15, and 22 m, respectively. The cross section at site D is asymmetrical, with the deepest point close to the eastern bank and a shelf of depth 10 m or less in the western half of the channel. The cross sections at sites B and C are more nearly symmetrical. The channel width is approximately 1 km at all three sites. The tidal excursion $2\hat{u}/\omega$, where \hat{u} and ω are the amplitude and radian frequency of the predominantly semidiurnal depth-averaged tidal current, varies between approximately 8 km during the weakest neap tides and 15 km during the strongest spring tides. The fluvial discharge during the measurement period, averaged over the cross section at the central C site, corresponded to a velocity of roughly 0.01 m s^{-1} , much smaller than the tidal velocities (section 3b).

Fixed instrumentation was concentrated at the central C site (Fig. 2). At this site, a bottom quadrupod supported five benthic acoustic stress sensors (BASS), which provide acoustic travel-time measurements of the three-dimensional velocity vector in a sample volume with a scale of 0.15 m (Williams et al. 1987). The quadrupod also supported three Seabird temperature sensors, five Seabird conductivity sensors, four Downing and Associates optical backscatter sensors (OBS), a ParoScientific pressure sensor, and a compass and tilt sensors. The BASS were at heights of 0.28, 0.58, 1.18, 2.08, and 2.73 m above bottom, the conductivity and OBS were at the same heights as the BASS, and the temperature sensors were at heights of 0.28, 1.18, and 2.73 m. The quadrupod was designed so that flow disturbances were well cross-stream of the sensors, and care was taken during deployment to ensure proper alignment of the quadrupod with respect to the nearly rectilinear tidal flow. A surface mooring at the central site supported an InterOcean S4 current meter fitted with conductivity and pressure sensors, at a depth of 2.7 m below the surface; four Seabird temperature–conductivity sensors fitted with OBS, at depths of 4.3, 6.3, 8.3, and 10.3 m; and a Seabird temperature–conductivity sensor fitted with a pressure sensor, at a depth of 12.3 m. A bottom tripod at the central site supported a 1200 kHz, narrowband, upward-looking acoustic Doppler current profiler (ADCP), manufactured by RD Instruments, and a Seabird temperature–conductivity sensor fitted with a pressure sensor. On the tripod, the Seabird sensors and the ADCP transducers were 0.5 m above bottom.

Supporting instrumentation was deployed at secondary sites A, B, D, E, and F (Fig. 2). At each of the secondary sites, a bottom tripod supported a Seabird temperature–conductivity sensor fitted with a ParoScientific pressure sensor. The tripods at sites D, E, and F also supported S4 current meters, and surface moorings at sites E and F supported Seabird temperature–conductivity sensors fitted with OBS.

All of the fixed instruments except those on the bottom quadrupod recorded averaged values of rapidly sampled measurements at intervals of 5, 10, or 20 min. Measurements on the quadrupod were sampled and recorded at a rate of approximately 6 Hz in one burst of length 3.28 min (first BASS deployment) or 6.29 min (second BASS deployment) every 10 min.

The measurement period extended from 15 August to 26 October 1995. The central mooring, the ADCP tripod, and the tripods and moorings at the secondary sites were on station during the entire measurement period. The BASS quadrupod was on site during two shorter intervals at the beginning and end of the measurement period. The first, termed BASS-1, was from 16 to 30 August, and the second, termed BASS-2, was from 17 to 26 October.

With few exceptions, the fixed instruments functioned well. At the central site, the S4 and accompanying conductivity sensor at the topmost position on the surface mooring fouled rapidly and did not produce useful measurements. The conductivity sensors on the bottom quadrupod indicated substantial intermittent reductions in conductivity, apparently

associated with fouling by suspended sediment. By removing these features, we obtained near-bottom salinity records with meaningful temporal variability, indicated by good agreement with shipboard measurements and with salinity records from the mooring, but the uncertainties were too large to permit meaningful direct estimates of the weak near-bottom stratification. At the top four BASS, the inclination of the velocity vector in the x - z plane, indicated by the ensemble of hour-averaged velocities, is within 1° of the inclination indicated by the pitch sensor. At the bottom BASS, hour-averaged velocities indicate a persistent downward flow at an angle of approximately 3° during both flood and ebb, possibly due to a slight local flow disturbance. The ADCP measurements, sampled in 1-m bins extending from 1.5 to 15.5 m above bottom, were degraded severely by surface contamination in the top four bins. In addition, ADCP measurements of velocity in the lowest two bins were substantially larger than BASS velocities at comparable heights and also substantially larger than a downward extrapolation of the other ADCP measurements, which indicates flow distortion by the ADCP tripod. Consequently, we use only the ADCP measurements in bins between 3.5 and 11.5 m above bottom.

Shipboard measurements complemented the fixed, time series measurements. Shipboard instrumentation included a Klein sidescan sonar, operating at 100 and 500 kHz; a downward-looking, 1200 kHz, narrowband ADCP, manufactured by RD Instruments; and a conductivity–temperature–depth (CTD) profiler, manufactured by Ocean Sensors, fitted with a Downing and Associates OBS. A sidescan sonar survey on 15 August focused on a region spanning most of the channel width with a length of 2 km in the along-channel direction, near the central site. A set of periodic surveys resolved the tidal and vertical structure of velocity, salinity, and turbidity along three cross-channel transects, coinciding in along-channel position with sites B, C, and D on 18 and 28 August, and 19, 21, and 23 October. A second set of periodic surveys resolved the tidal and vertical variability of the same quantities along a 28-km along-channel transect on 17 and 27 August and 18, 20, and 22 October.

b. Analysis

The purpose of the analysis was to obtain hour-averaged estimates of the quantities in (1) through (3) at the central C site. The required quantities are $-\overline{u'w'}$, $\partial u/\partial z$, ϵ , τ_b , $\partial u/\partial t$, $\partial p/\partial x$, and, for the purposes of the discussion (section 4), $\partial \rho/\partial z$, where $\rho(x, z, t)$ is density.

To obtain hour-averaged estimates of $-\overline{u'w'}$, we divided velocity measurements from each BASS into one-hour segments, each consisting of six bursts. We demeaned and removed a linear trend (in time) from the measurements in each segment and then computed the covariance of the demeaned and detrended along-channel and vertical velocities. The resulting stress estimates contain contributions from velocity fluctuations limited at low frequencies by the detrending operation on the one-hour segments, and at high frequencies by the finite sample volume of the BASS, which attenuate fluctuations with spatial scales smaller than the 0.15-m length of the acoustic paths. Quantitative calculations of the effect of the spatial filtering on stress estimates do not exist, but calculations for isotropic turbulence, based on a line-average model of the sample volume (Kaimal et al. 1968), indicate that for acoustic paths inclined at 45° with respect to the along-channel flow, as in the present case, the half-power point of the spatial filtering is at $ka \approx 4.6$, where k is alongstream wavenumber and a is the pathlength. These results, combined with empirical expressions for the cospectrum of horizontal and vertical velocity in the unstratified wall region of the atmospheric surface layer (Kaimal et al. 1972), indicate that the frequency content of the present estimates is sufficient to resolve all but a few percent of the Reynolds stress, except near slack water. Uncertainties of stress estimates due to uncertainties in reference frame orientation are less than 10%, except at the lowest BASS, where hour-averaged velocities indicate a slight downward flow (section 2a). For this sensor, rotation into a coordinate frame aligned with the streamlines indicated by the ensemble of hour-averaged velocities changes stress estimates by approximately 20%, which has a negligible effect on the overall results.

We obtained hour-averaged values of the bottom stress by linearly regressing hour-averaged estimates of $-\rho_0 \overline{u'w'}$ at all five BASS against z and then using the results of the regression to extrapolate the stress to the seafloor. The estimates of Reynolds stress have little vertical structure so that extrapolation to the seafloor produces values of bottom stress that do not differ substantially from the array average.

We obtained hour-averaged estimates of ϵ at each of the top two BASS sensors by fitting spectra of along-channel velocity to the inertial-range model, $S_{uu}(k) = (9/55)\alpha\epsilon^{2/3}k^{-5/3}$ (Batchelor 1953). Here $S_{uu}(k)$ is the two-sided wavenumber spectrum of along-channel velocity, defined so that $\int_{-\infty}^{+\infty} S_{uu}(k) dk$ is variance; k is along-channel wavenumber, estimated from frequency f by means of the frozen-turbulence hypothesis ($k = 2\pi f/U$, where U is magnitude of the hour-averaged along-channel velocity); and α is the empirical Kolmogorov constant, approximately equal to 1.5 (Grant et al. 1962). For each burst from each of the top two BASS, we demeaned and detrended measurements of along-channel velocity, applied a Hanning window, and computed a two-sided frequency spectrum. We then averaged spectra from six adjacent bursts and multiplied by $U/(2\pi)$ to obtain an hour-averaged wavenumber spectrum. We estimated hour-averaged values of $\epsilon^{2/3}$ and a spectral noise level by fitting hour-averaged wavenumber spectra in the range $10/z \leq k \leq 2/a$, where $a = 0.15$ m is length of the BASS acoustic paths, to the inertial-range model, modified to include effects of aliasing, spatial

filtering (Kaimal et al. 1968), and a white noise floor. Finally, we raised estimates of $\epsilon^{2/3}$ to the 3/2 power to obtain hour-averaged estimates of dissipation.

The estimation procedure for ϵ is based on several considerations. We limited the model fit to $k > 10/z$ because measurements in the unstratified wall region of the atmospheric surface layer indicate that the inertial-range model is valid in this range (Kaimal et al. 1972), and to $k < 2/a$ because the computed effect of spatial filtering on spectral density is less than 20% in this range. We computed dissipation estimates only for the top two BASS because the range $10/z \leq k \leq 2/a$ is nonexistent for the bottom two sensors and so narrow for the third sensor that estimates of $\epsilon^{2/3}$ are extremely noisy and occasionally negative. We did not compute dissipation estimates from spectra of vertical velocity because these spectra were not consistent with inertial-range behavior except at wavenumbers so large that the eddy scale was comparable to the scale of the BASS sample volume (section 3a). We computed dissipation estimates from spectra of cross-channel velocity, but we do not present them here because they are well correlated and consistent in magnitude with estimates obtained from along-channel velocity.

The along-channel pressure gradient can be expressed as the sum of the bottom pressure gradient and a baroclinic correction due to the along-channel density gradient:

$$\frac{\partial p}{\partial x} = \left(\frac{\partial p}{\partial x} \right)_{z=0} - g \int_0^z \frac{\partial \rho}{\partial x} dz, \quad (4)$$

where $z = 0$ coincides with the seafloor, as before, and g is gravitational acceleration. To estimate the bottom pressure gradient at the central C site, we computed a finite-difference approximation by using near-bottom time-series measurements of pressure at sites B and D, and we corrected for the difference in height of the two sensors by using time series measurements of density at the two sites. To obtain a crude estimate of the baroclinic term in (4), we assumed that $\partial \rho / \partial x$ is independent of z , and we computed a finite-difference approximation to $\partial \rho / \partial x$ by using near-bottom time-series measurements of density at sites B and D. These calculations indicate that tidal fluctuations (predominantly semidiurnal with a smaller diurnal component) produce approximately 97% of the variance of bottom pressure gradient. The baroclinic term in (4) produces a negligible fraction (approximately 1%) of the tidal variance of pressure gradient, but it produces a significant fraction of the much smaller subtidal variance. The measurements are insufficient to determine the mean of the pressure gradient, which would require knowledge of the relative heights of the pressure sensors at sites B and D with an uncertainty on the order of 0.001 m.

To avoid uncertainties associated with estimates of the mean and baroclinic pressure gradients in our examination of (3), we focused on the tidal dynamics, which dominate the variance, by high-pass filtering the terms in this equation. We computed high-pass filtered quantities by subtracting the corresponding low-pass filtered record, computed by means of filter p164 (e.g., Limeburner 1985), which removes diurnal and semidiurnal fluctuations and has a half-power point at a period of approximately 1.5 days. As well as removing the mean, this operation removes effects of the baroclinic pressure gradient, which contributes negligibly at tidal frequencies.

To estimate near-bottom values of $\partial \rho / \partial z$ at two heights above bottom (approximately 0.7 and 2.0 m), we computed finite difference approximations to $\partial T / \partial z$, where T is temperature, based on the bottom and top pairs of temperature sensors on the quadrapod and applied a temperature–density relationship obtained by regressing $\partial \rho / \partial t$, averaged over the quadrapod array, against $\partial T / \partial t$, also averaged over the quadrapod array. The temperature–density relationship determined in this way was well defined (the squared correlation coefficient r^2 for array-averaged $\partial \rho / \partial t$ and $\partial T / \partial t$ was 0.82 for all of BASS-1 and the first half of BASS-2 and it was 0.68 for the second half of BASS-2). We used indirect estimates of $\partial \rho / \partial z$ because the quadrapod conductivity measurements were sufficient to determine the temporal variability of density but insufficient, due to drift and noise, to determine the much weaker vertical variability, as noted in section 2a. In contrast, the near-bottom temperature measurements indicated a coherent vertical structure (the squared correlation coefficient r^2 for the two estimates of $\partial T / \partial z$ was 0.79 for BASS-1 and 0.74 for BASS-2), and, as expected, they indicated predominantly stable or neutrally stratified near-bottom conditions, with rare, brief occurrences of weak unstable stratification, primarily during flooding spring tides. Analysis of OBS measurements indicates that suspended sediment contributed negligibly to near-bottom stratification.

The remainder of the analysis is straightforward. We computed $\partial u / \partial t$ by using centered differences of hour-averaged BASS and ADCP velocity measurements. We used a midpoint rule to evaluate the integral in (3). Our estimates of $\partial u / \partial z$ are described in section 3b.

3. Results

a. General characteristics of the measurements

Before proceeding to an examination of (1)–(3), a preliminary presentation of the measurements is instructive. Here we summarize briefly the results of the side-scan survey, we describe the temporal and vertical variability of velocity and salinity, and we present representative spectra and cospectra of along-channel and vertical velocity.

The sidescan survey (Fredericks et al. 1998) indicated a generally featureless seafloor, although there were differences in texture shown by concurrent grab samples to be indicative of coarse, nonerodible material near the center of the channel and soft, unconsolidated sediment near the western bank. The survey also indicated a partially buried pipe, which crossed the entire channel approximately 150 m to the south of the central site (Fig. 1), producing relief up to roughly 1 m.

The measurements indicate that the amplitude of the tidal sea level fluctuations at the central site varied between approximately 0.4 m during the weakest neap tides and 0.8 m during spring tides. Pressure fluctuations were nearly in phase (within one hour) with sea level fluctuations, indicating that the tide at the central site is a progressive wave, with maximum flooding and ebbing tidal currents corresponding to high and low water, respectively.

Time series of near-surface and near-bottom along-channel velocity (Figs. 3a and 3b), together with time series of the difference between near-bottom and near-surface salinity (Fig. 3c), indicate dominant tidal variability with weak fortnightly modulation, stronger monthly modulation, and strong vertical gradients of along-channel velocity. The near-surface tidal velocity varies from roughly $\pm 1.2 \text{ m s}^{-1}$ during spring tides to roughly $\pm 0.6 \text{ m s}^{-1}$ during the weakest neap tides (Fig. 3a). The near-bottom tidal velocity is much weaker (Fig. 3b). The subtidal top-to-bottom salinity difference varies between roughly 1 psu during the strongest spring tides to roughly 4 psu during the weakest neap tides (Fig. 3c). The time series indicate fairly regular fortnightly and monthly modulation, except for an event near the end of the record (yeardays 293 to 298) corresponding to a period of high river discharge, in which a brief period of strong seaward flow near the bottom (Fig. 3b) was followed by strong stratification (Fig. 3c) in spite of strong spring tidal velocities (Fig. 3a). The tidal and subtidal velocities are strongly rectilinear with transverse velocities approximately 10% of along-channel velocities.

Statistics of velocity and salinity during BASS-1, which spanned a two-week period during the beginning of the experiment (Fig. 3b), illustrate the vertical structure of the flow and density fields. The mean salinity profile during both neap (the first half of BASS-1) and spring tides (the second half of BASS-1) indicate no stratification within 3 m of the seafloor (Figs. 4a and 4b). Stratification is apparent during both spring and neap tides at heights greater than 5 m above bottom, and the strongest mean stratification, observed during neap tides, occurs within 5 m of the surface. The stratification is nearly in quadrature with the velocity so that the salinity distributions during maximum flood and ebb are nearly equal to the mean salinity distribution. Velocities during the ebbing tide, averaged over the entire two-week period, indicate a smooth transition between BASS and ADCP velocities and strong shear throughout the entire water column (Fig. 4c). In contrast, corresponding velocities during flooding tide (Fig. 4c) indicate a subsurface maximum at a height of approximately 10 m above bottom. In addition, a slight discontinuity occurs during flooding tide between BASS and ADCP velocities, possibly caused by the partially buried pipe south of the central site (section 2a) or the fact that the BASS and ADCP sensors were separated by approximately 200 m in the cross-channel direction (section 2a). The ADCP velocity profiles are slightly jagged, with good correlation between velocities in alternate bins and offsets between velocities in adjacent bins (Fig. 4c). This feature is likely a result of the processing internal to the ADCP (T. Chereskin 1998, personal communication) and it has no effect on the present results.

In Fig. 3c, the mean velocity (i.e., averaged over the entire two-week period of the first BASS deployment) is landward near the bottom and seaward near the surface. This sheared exchange flow, which is a dominant feature of the subtidal velocity field and is likely instrumental in accomplishing the horizontal flux of salt into the estuary, is driven by the combination of barotropic and baroclinic pressure gradients, as described classically by Pritchard (1956). The estuarine exchange flow has pronounced monthly variability, similar to the stratification (Fig. 3c), with strong pulses during periods of weakest stratification. An analysis of the dynamics of the subtidal exchange flow in the Hudson estuary, based on the measurements described here, is reported by Geyer et al. (2000).

Representative spectra and cospectra of along-channel and vertical velocities are approximately consistent with expectations based on measurements in the neutrally stratified wall region of the atmospheric surface layer (Fig. 5). The spectrum $S_{uu}(k)$ of along-channel velocity indicates the inertial-range behavior $S_{uu}(k) \propto k^{-5/3}$ over a broad range of wavenumbers greater than $k \approx 1/z$ (Fig. 5a). In contrast, spectral density $S_{ww}(k)$ of vertical velocity is not proportional to $k^{-5/3}$ and is smaller than the isotropic relationship $(3/4)S_{ww} = S_{uu}$ (e.g., Batchelor 1953) except at wavenumbers so large that the eddy scale is comparable to the length of the BASS acoustic paths (Fig. 5a). The spectrum of vertical velocity is consistent, given the observed value of $-u'w'$ (obtained by integrating the cospectrum in Fig. 5b), with an empirical expression obtained in the unstratified atmospheric surface layer (Kaimal et al. 1972). The spectrum of along-channel velocity is consistently slightly larger than the empirical expression except at large wavenumbers. The cospectrum $C_{uw}(k)$ of

along-channel and vertical velocities (Fig. 5b) indicates a slight shift of cospectral density to higher wavenumbers than observed in the atmosphere (Fig. 5b), possibly indicating a slight suppression of the turbulent length scale.

b. Turbulent energy balance, law of the wall, and momentum balance

To obtain a concise representation of the approximate turbulence energy equation (1) at the top two BASS (the only sensors where we obtained dissipation estimates), we averaged the values of dissipation at the two sensors, and we obtained a corresponding value of production by averaging the estimates of $-u'w'$ at the two sensors and then multiplying by an estimate of $\partial u/\partial z$ based on the difference between the velocity measurements at the two heights. The resulting values of production and dissipation are well correlated (squared correlation coefficient $r^2 = 0.81$ for BASS-1 and 0.46 for BASS-2) and nearly equal in magnitude (Figs. 6a and 7a), which is consistent with expectations for a nearly unstratified wall region in a turbulent boundary layer (e.g., Tennekes and Lumley 1972). Scatterplots of production versus dissipation (Figs. 6b, 6c, 7b, and 7c) indicate substantial sampling variability, particularly during BASS-2, but systematic differences are small except at values of production less than approximately $10^{-6} \text{ W kg}^{-1}$, where the results suggest an effective noise level in the dissipation estimates. Production and dissipation are larger during spring tides than during neap tides, and both are well correlated with the cube of the along-channel velocity averaged over the BASS array ($r^2 = 0.55$ for production and 0.80 for dissipation for BASS-1 and BASS-2 combined), which is consistent with a simple model in which $\tau_b \propto |u|$, $\partial u/\partial z \propto u$, and $\epsilon \propto |u|^3$. Although these proportionality relationships are consistent with the law of the wall, the quantitative ratio of $z\partial u/\partial z$ to $|\tau_b/\rho_0|^{1/2} \text{sgn}(\tau_b)$ is, for the most part, inconsistent with the law of the wall (see below). Dissipation estimates obtained from spectra of cross-channel velocity, instead of along-channel velocity (section 2b), are in slightly better agreement with values of production than are the dissipation estimates in Figs. 6 and 7.

To obtain a concise representation of the law of the wall (2), we regressed hour-averaged values of u at the bottom three BASS and at the top three BASS against $\log(z)$, to obtain $z\partial u/\partial z = \partial u/\partial[\log(z)]$ at two heights, corresponding approximately to $z = 0.7 \text{ m}$ (the mean height of the bottom three BASS) and $z = 2.0 \text{ m}$ (the mean height of the top three BASS). This procedure permits examination of the vertical structure of $z\partial u/\partial z$ while reducing substantially the sampling variability associated with estimates based on measurements at only two BASS. Plots of $\kappa z\partial u/\partial z$ as a function of $|\tau_b/\rho_0|^{1/2} \text{sgn}(\tau_b)$ indicate straight-line relationships through the origin (Fig. 8), which is qualitatively consistent with (2). To quantify this information, we defined

$$\phi_m = \frac{\kappa z}{|\tau_b/\rho_0|^{1/2}} \text{sgn}(\tau_b) \frac{\partial u}{\partial z}, \quad (5)$$

following the notation in the atmospheric literature (e.g., Businger et al. 1971), so that $\phi_m = 1$ corresponds to the law of the wall. We estimated ϕ_m and corresponding 95% confidence intervals by regressing $\kappa z\partial u/\partial z$ against $|\tau_b/\rho_0|^{1/2} \text{sgn}(\tau_b)$, assuming Gaussian statistics. The results indicate consistency with the law of the wall during flooding tide (corresponding to $\tau_b > 0$) at the lowest elevation ($z = 0.7 \text{ m}$) resolved by this procedure (Figs. 8a and 8c). At greater heights and at all elevations during ebbing tide, ϕ_m is significantly greater than unity, indicating departures from the law of the wall in a manner consistent with stable stratification (e.g., Monin and Yaglom 1971). Results for spring tides and neap tides do not differ substantially (Fig. 8), although there is consistently more scatter in plots of $\kappa z\partial u/\partial z$ as a function of $|\tau_b/\rho_0|^{1/2} \text{sgn}(\tau_b)$ during spring tides.

As described in section 2b, we filtered the terms in the momentum balance to focus on the dominant tidal variability and to remove uncertainties associated with estimation of the mean and baroclinic pressure gradients. This filtering operation has been applied to all terms in (3) that are presented in the following.

Before proceeding to the complete momentum balance, an examination of $\rho_0 \partial u/\partial t + \partial p/\partial x$, the left side of the frictionless differential momentum equation corresponding to (3), is instructive. Because the velocity is dominated by the semidiurnal tide, $\rho_0 \partial u/\partial t$ is nearly identical in magnitude to $\rho_0 \omega u$, where $\omega = 1.41 \times 10^{-4} \text{ s}^{-1}$ is radian frequency, as in section 2a. The quantity $\rho_0 \omega u$ has weak fortnightly and stronger monthly modulation, and near the surface it varies by a factor of ~ 2 , between roughly $\pm 0.14 \text{ Pa m}^{-1}$ during spring tides and roughly $\pm 0.07 \text{ Pa m}^{-1}$ during the weakest neap tides (Fig. 3a). In contrast, the quantity $\rho_0 \partial u/\partial t + \partial p/\partial x$ has stronger fortnightly and pronounced monthly modulation, particularly near the surface, where it varies by an order of magnitude, between roughly $\pm 0.1 \text{ Pa m}^{-1}$ during spring tides and $\pm 0.01 \text{ Pa m}^{-1}$

during the weakest neap tides (Fig. 9a). At greater depths, the monthly modulation is less pronounced and $\rho_0 \partial u / \partial t + \partial p / \partial x$ reaches roughly $\pm 0.05 \text{ Pa m}^{-1}$ during the weakest neap tides (Figs. 9b and 9c).

Estimates of $\int_0^h (\rho_0 \partial u / \partial t + \partial p / \partial x) dz$, the depth integral of the quantity in Fig. 9, are well correlated with direct covariance estimates of τ_b obtained from the BASS velocity measurements (Figs. 10a and 11a). The magnitudes of these quantities agree reasonably well during the neap-tide period of BASS-1 (Fig. 10b), particularly between days 231 and 235 (Fig. 10a). During the spring-tide period of BASS-1 and during all of BASS-2, estimates of τ_b are systematically smaller than estimates of $\int_0^h (\rho_0 \partial u / \partial t + \partial p / \partial x) dz$, by a factor of roughly up to 2 (Figs. 10c, 11b, and 11c). Measurements obtained during the two spring-tide periods indicate a similar relationship between $\int_0^h (\rho_0 \partial u / \partial t + \partial p / \partial x) dz$ and τ_b (Figs. 10c and 11c). In contrast, measurements obtained during the two neap-tide periods indicate two different relationships between these quantities (Figs. 10b and 11b).

In Figs. 10 and 11, estimates of $\int_0^h (\rho_0 \partial u / \partial t + \partial p / \partial x) dz$ and $-\tau_b$ are in slightly better agreement during neap tides than during spring tides. This statement is clearly consistent with the BASS-1 results, and it is less clear but still consistent with the BASS-2 results. It is instructive to extend this result in an approximate way to the entire two-month period of the ADCP and pressure measurements, by introducing a quadratic drag law to relate the bottom stress to the ADCP velocity measurement at $z = 3.5 \text{ m}$. Combined results for BASS-1 and BASS-2 indicate that BASS covariance estimates of τ_b and the ADCP measurement of $u|u|$ at $z = 3.5 \text{ m}$ are well correlated (squared correlation coefficient $r^2 = 0.86$), and that the drag coefficient c_d in the relationship $\tau_b = c_d \rho_0 u|u|$ is approximately 1.7×10^{-3} , with no significant differences between neap and spring tides. To determine amplitudes of tidal fluctuations, we square estimates of $\int_0^h (\rho_0 \partial u / \partial t + \partial p / \partial x) dz$ and τ_b , apply low-pass filter p164, and take the square root. The results (Fig. 12), indicate good agreement between amplitudes of stresses based on BASS covariance estimates and the drag law, as expected, and they also indicate that the closest agreement between the drag law and $\int_0^h (\rho_0 \partial u / \partial t + \partial p / \partial x) dz$ occurs during the periods with the strongest stratification, near days 230, 260, and 290, with the greatest discrepancies during the periods of weakest stratification (see Fig. 3c).

4. Discussion

a. Turbulent kinetic energy balance

The good agreement in Figs. 6 and 7 between estimates of production and dissipation implies a specific, quantitative relationship between the cospectrum of along-channel and vertical velocities at values of $2\pi fz/U$ between roughly 0.1 and 10 (the scales that contribute to $u'w'$), the spectrum of along-channel velocity at values of $2\pi fz/U$ greater than 10 (the range of scales that coincides approximately with the inertial subrange and leads to estimates of ϵ), and the part of the along-channel velocity spectrum that contributes to variability of hour-averaged values of $\partial u / \partial z$. The quantitative consistency indicated in Figs. 6 and 7 between spectra and cospectra at these disparate ranges of frequency suggests that turbulence statistics obtained from the BASS measurements are reasonably accurate.

b. Law of the wall

Possible explanations of observed departures from the law of the wall except at the lowest resolved elevation during flooding tide (Fig. 8) include temporal acceleration of the tidal flow (Soulsby and Dyer 1981); advective acceleration over variable topography (e.g., Smith and McLean 1977); stratification due to heat, salt, or suspended sediment (e.g., Monin and Yaglom 1971); and finite boundary layer thickness (Coles 1956).

The effect of temporal acceleration on the velocity profile has a different sign during acceleration and deceleration, and it is zero at maximum velocity. In contrast, the present measurements do not indicate substantial differences between accelerating and decelerating phases of the tide and they do not indicate convergence to $\Phi_m = 1$ at maximum velocity (Fig. 8). Thus temporal acceleration of the tidal flow does not explain the observed departures from the law of the wall.

The coarse bottom material at the central measurement site does not suggest substantial dunes or large-scale ripples (e.g., Allen 1984), and the sidescan survey indicated no significant topographical features except for the partially buried pipe south of the central site (section 3a). Flow distortion by the pipe might explain some of the observed departure from the law of the wall at $z \approx 2 \text{ m}$ during flooding tide (Figs. 8b and 8d), but it does not explain departures from the law of the wall during ebbing tide.

The effect of stable stratification can be estimated by means of the Monin–Obukhov theory (e.g., [Monin and Yaglom 1971](#)), which addresses the effect on the constant-stress layer of a vertically uniform buoyancy flux $(g/\rho_0)\overline{\rho'w'}$, where ρ' denotes turbulent density fluctuations. Strictly speaking, this theory does not apply to the present case, in which vertical fluxes of heat and salt must be negligible at the seafloor, so that $(g/\rho_0)\overline{\rho'w'}$ must vary with z if it is significant in the water column. However, application of the theory likely produces reasonable results if one uses the local value of $\overline{\rho'w'}$ in the calculations. This approach produces expressions that are quantitatively consistent with the level-2 turbulence model developed by [Mellor and Yamada \(1974, 1982\)](#), which is intended to apply to a broad class of boundary layer flows. The Monin–Obukhov theory leads to $\Phi_m = \Phi_m(\zeta)$, where Φ_m is the dimensionless shear introduced in [section 3b](#), and

$$\zeta = \frac{\kappa z}{|\tau_b/\rho_0|^{3/2}} \frac{g}{\rho_0} \overline{\rho'w'}. \quad (6)$$

Because we did not measure $\overline{\rho'w'}$ in the present study, we cannot compute ζ directly, and it is necessary to express the effect of stratification in terms of the gradient Richardson number Ri , defined by

$$Ri = \frac{-(g/\rho_0)(\partial\rho/\partial z)}{(\partial u/\partial z)^2}, \quad (7)$$

which is, in the Monin–Obukhov theory, an empirical function of ζ . Several atmospheric studies have produced estimates of the empirical functions $\Phi_m(\zeta)$ and $Ri(\zeta)$ [see [Hogstrom \(1988\)](#) for a review]. Here we use the results of [Businger et al. \(1971\)](#), which are, for stable stratification,

$$\Phi_m = 1 + \beta\zeta \quad (8)$$



and


$$Ri = \frac{\zeta(\gamma + \beta\zeta)}{(1 + \beta\zeta)^2}, \quad (9)$$

where β and γ are empirical constants, equal to approximately 4.7 and 0.74, respectively. These equations can be combined to yield

$$\Phi_m = \frac{2 - \gamma + [\gamma^2 + 4(1 - \gamma)\beta Ri]^{1/2}}{2(1 - \beta Ri)}. \quad (10)$$

According to this expression, $\Phi_m = 1$ at $Ri = 0$, and $\Phi_m \rightarrow +\infty$ at a critical value of Ri equal to $1/\beta$, at which the turbulent momentum flux vanishes.

To apply (7) and (10) at heights of approximately 0.7 and 2.0 m above bottom, we estimated $\partial\rho/\partial z$ as described in [section 2b](#), and we estimated shear by regressing u against $\log(z)$ for the bottom three and top three BASS, as explained in [section 3b](#), and dividing the resulting estimates of $z\partial u/\partial z$ by the average value of z . Values of Ri obtained from this procedure are order unity or larger at all heights during slack water when shears are weak and stratification is strong. In contrast, at the lowest resolved height (0.7 m) during maximum flood and maximum ebb, estimates of Ri are sufficiently small (roughly 0.003) that (10) indicates a small departure (approximately 2%) from the law of the wall, much smaller than the observed departure at this height during ebbing tide ([Fig. 8](#) ). At the highest resolved height (2.0 m) during maximum flood and maximum ebb, estimates of Ri are larger (roughly 0.02), but the departure from the law of the wall indicated by (10) (approximately 15%) remains smaller than the observed departure ([Fig. 8](#) ). Thus stable stratification might have an influence on the velocity structure at the largest heights within the BASS array, but it is not the dominant effect producing departures from the law of the wall.

The most likely explanation of the observed departures from the law of the wall is finite thickness of the relatively well-mixed region below the pycnocline, which is at most a few meters ([Figs. 4a,b](#) ). Finite thickness of a turbulent flow is known to increase shear for fixed stress relative to the law of the wall, consistent with $\Phi_m > 1$ ([Coles 1956](#)). This effect is difficult to quantify in the present application, but crude estimates can be obtained from [Coles' \(1956\)](#) empirical expression for a steady unstratified boundary layer, which leads to

$$\frac{\kappa z}{|\tau_b/\rho_0|^{1/2}} \operatorname{sgn}(\tau_b) \frac{\partial u}{\partial z} = 1 + \Pi \left(\frac{\pi z}{\delta} \right) \sin \left(\frac{\pi z}{\delta} \right), \quad (11)$$

where δ is boundary layer thickness and Π is the empirical Coles parameter, dependent on the externally applied streamwise pressure gradient and approximately equal to 0.55 at zero pressure gradient. Although (11) does not reproduce quantitatively the vertical structure of the departure from the law of the wall observed here, it indicates (with $\Pi = 0.55$) a maximum value of approximately 2 at $z/\delta \approx 0.63$, which is comparable to the observed behavior in Fig. 8 if δ is a few meters.

c. Momentum balance

A possible explanation of the differences between estimates of $\int_0^h (\rho_0 \partial u / \partial t + \partial p / \partial x) dz$ and $-\tau_b$ (Figs. 10 and 11) is measurement problems. In particular, if one could show that the present direct covariance estimates of stress are in error and should be multiplied by 2, then the resulting overall agreement between $\int_0^h (\rho_0 \partial u / \partial t + \partial p / \partial x) dz$ and $-\tau_b$ would be substantially better than in Figs. 10 and 11. This operation would, however, degrade the excellent agreement indicated by the present estimates between days 231 and 235 (Fig. 10a), and it would not change the variability of the relationship between amplitudes of $\int_0^h (\rho_0 \partial u / \partial t + \partial p / \partial x) dz$ and $-\tau_b$ (Fig. 12). In addition, the a priori assessment of the quality of the stress estimates (section 2b), the successful closure of the turbulent energy balance (Figs. 6 and 7), and the observed coincidence with the law of the wall near the seafloor during flooding tides (Figs. 8a and 8c) suggest that the present estimates of turbulence statistics based on the BASS measurements are reasonably accurate. Similarly, the observed near cancellation of $\rho_0 \partial u / \partial t$ and $-\partial p / \partial x$ near the surface during the weakest neap tides (Fig. 9a) indicates that the present estimates of these quantities are accurate. Some of the discrepancies in the momentum balance might be caused by the cross-channel separation of the BASS and ADCP measurements (Fig. 2). However, the best agreement between the topmost BASS and lowest ADCP velocity measurements (within approximately 10% in amplitude) occurs during weak stratification, which does not explain the fact that the best closure of the momentum balance occurs during strong stratification.

A second issue related to the comparison of $\int_0^h (\rho_0 \partial u / \partial t + \partial p / \partial x) dz$ and $-\tau_b$ is that of spatial scales. We obtained estimates of pressure gradient from measurements of bottom pressure separated by an along-channel distance of approximately 7 km (Fig. 1), and values of $\partial u / \partial t$ summed over the 15-m water column are influenced by along-channel spatial scales up to the tidal excursion, which is 8 to 15 km (section 2a). In contrast, we obtained local estimates of $-\tau_b$ at the central site from measurements within 3 m of the seafloor of velocity fluctuations with spatial scales on the order of meters. If there is substantial along-channel variability of bottom stress on a scale of kilometers (caused, for example, by spatial variations of bottom roughness) or if a significant fraction of the momentum transfer to the seafloor is transmitted by form drag on localized obstacles, then there will be disagreement between estimates of $\int_0^h (\rho_0 \partial u / \partial t + \partial p / \partial x) dz$, as we have obtained them, and local estimates of the turbulent Reynolds stress. These ideas are difficult to test with the present observations. However, neither idea obviously explains the observation (Fig. 12b) that estimates of $\int_0^h (\rho_0 \partial u / \partial t + \partial p / \partial x) dz$ and $-\tau_b$ are in better agreement during periods of strong stratification than during periods of weak stratification. In particular, one would expect form drag to increase, rather than decrease, with increasing stratification because of the increased chance for internal hydraulic phenomena (e.g., jumps formed by localized obstacles) to dissipate energy.

A final issue related to the comparison of $\int_0^h (\rho_0 \partial u / \partial t + \partial p / \partial x) dz$ and $-\tau_b$ is that of momentum transfer represented by the advective terms that are neglected in (3). Significant momentum transport represented by these terms could be produced by transverse, secondary flows. For example, the quantity $\int_0^h \rho_0 w \partial u / \partial z dz$, one of the terms neglected in (3), would be $O(1 \text{ Pa})$ (the order of discrepancies in the momentum balance) with $h = O(10 \text{ m})$ and the observed $\partial u / \partial z = O(10^{-1} \text{ s}^{-1})$ if w were $O(10^{-3} \text{ m s}^{-1})$, corresponding (via the continuity equation) to $\mathbf{v} = O(5 \times 10^{-2} \text{ m s}^{-1})$, which is comparable to observed cross-channel velocities. Secondary flows in estuaries have been the subject of limited theoretical work (Smith 1976) and observational work (e.g., Nunes and Simpson 1985; Guymer and West 1991), primarily in well-mixed systems, and little is known about them in partially mixed systems. However, it is possible that these features have the strongest effect on the momentum balance during periods of weak stratification (which would be consistent with the results in Fig. 12b) because the associated vertical motions might be suppressed by strong stratification.

5. Summary and conclusions

We have presented measurements in a straight section of the partially mixed lower Hudson estuary that resolve the vertical structure of velocity and along-channel pressure gradient throughout the 15-m water column at a central measurement site, as well as providing direct covariance estimates of Reynolds stress and indirect inertial-range estimates of dissipation within 3 m of the seafloor. The analysis focuses on testing a simple turbulence energy budget, in which production balances dissipation, the Prandtl–Karman law of the wall, which relates velocity gradient to bottom stress, and a simplified depth-integrated along-channel momentum equation, involving temporal acceleration, pressure gradient, and bottom stress.

Estimates of turbulence production and dissipation agree well, indicating that measurements of velocity fluctuations at disparate timescales are related in a manner consistent with expectations based on previous measurements in other systems. These results suggest that the present estimates of turbulence statistics are reasonably accurate.

The observed relationship between velocity gradient and bottom stress is consistent with the law of the wall at the lowest resolved height during flooding tides, but it departs from the law of the wall at greater heights during flooding tides and at all resolved heights during ebbing tides. The observed behavior is qualitatively consistent with the effect of stable stratification, but the local stratification is too small to explain the effect. The likely explanation is the finite thickness of the relatively well-mixed layer below the pycnocline, which could suppress the turbulent length scale and therefore increase the velocity gradient for a fixed bottom stress.

Direct covariance estimates of bottom stress are well correlated with the sum of the other terms (the momentum integral) in the simplified along-channel momentum balance. The magnitude of the stress estimates is nearly equal to the magnitude of the momentum integral during brief periods, but more often it is smaller by a factor of up to roughly 2. Agreement between stress estimates and the momentum integral is best during periods of strongest top-to-bottom stratification, and it is worst during periods of weak stratification. This behavior, which might be related to spatial variability of bottom stress, form drag, or momentum transport by secondary flows, is not understood.

Acknowledgments

This study was supported by the National Science Foundation under Grant OCE-9415617. We thank Craig Marquette, Matthew Gould, and the captain and crew of research vessel *Onrust* for their excellent work during deployment and recovery. We also thank Janet Fredericks and Jonathan Woodruff for their preliminary processing of the data.

REFERENCES

- Allen, J. R. L., 1984: *Sedimentary Structures, Their Character and Physical Basis*. Elsevier, 589 pp..
- Batchelor, G. K., 1953: *The Theory of Homogeneous Turbulence*. Cambridge University Press, 197 pp..
- Bowden, K. F., 1962: Measurements of turbulence near the sea bed in a tidal current. *J. Geophys. Res.*, **67**, 3181–3186..
- , and L. A. Fairburn, 1952: Further observations of the turbulent fluctuations in a tidal current. *Philos. Trans. Roy. Soc. London A*, **244**, 335–356..
- , and —, 1956: Measurements of turbulent fluctuations and Reynolds stresses in a tidal current. *Proc. Roy. Soc. London A*, **237**, 422–438..
- Businger, J. A., J. C. Wyngaard, Y. Izumi, and E. F. Bradley, 1971: Flux–profile relationships in the atmospheric surface layer. *J. Atmos. Sci.*, **28**, 181–189.. [Find this article online](#)
- Coles, D., 1956: The law of the wake in the turbulent boundary layer. *J. Fluid Mech.*, **1**, 191–226..
- Draper, N. R., and H. Smith, 1966: *Applied Linear Regression*. John Wiley, 709 pp..
- Fredericks, J. J., J. H. Trowbridge, W. R. Geyer, A. J. Williams, M. Bowen, and J. Woodruff, 1998: Stress, salt flux and dynamics of a partially mixed estuary. Tech. Rep. WH01-98-17, Woods Hole Oceanographic Institution, 133 pp. [Available from Woods Hole Oceanographic Institute, Woods Hole, MA 02543.].
- Geyer, W. R., J. H. Trowbridge, and M. M. Bowen, 2000: The dynamics of a partially mixed estuary. *J. Phys. Oceanogr.*, in press..
- Gordon, C. M., 1974: Intermittent momentum transport in a tidal boundary layer. *Nature*, **248**, 392–394..
- , and C. F. Dohne, 1973: Some observations of turbulence in a tidal estuary. *J. Geophys. Res.*, **78**, 1971–1978..

- Grant, H. L., R. W. Stewart, and A. Moilliet, 1962: Turbulence spectra from a tidal channel. *J. Fluid Mech.*, **12**, 241–263..
- , A. J. Williams, and S. M. Glenn, 1984: Bottom stress estimates and their prediction on the northern California shelf during CODE-1: The importance of wave–current interaction. *J. Phys. Oceanogr.*, **14**, 506–527.. [Find this article online](#)
- Green, M. O., 1992: Spectral estimates of bed shear stress at subcritical Reynolds numbers in a tidal boundary layer. *J. Phys. Oceanogr.*, **22**, 903–917.. [Find this article online](#)
- , and I. N. McCave, 1995: Seabed drag coefficient under tidal currents in the eastern Irish Sea. *J. Geophys. Res.*, **100**, 16 057–16 069..
- Gross, T. F., and A. R. M. Nowell, 1983: Mean flow and turbulence scaling in a tidal boundary layer. *Contin. Shelf Res.*, **2**, 109–126..
- , and —, 1985: Spectral scaling in a tidal boundary layer. *J. Phys. Oceanogr.*, **15**, 496–508.. [Find this article online](#)
- , A. J. Williams, and W. D. Grant, 1986: Long-term in-situ calculations of kinetic energy and Reynolds stress in a deep sea boundary layer. *J. Geophys. Res.*, **91**, 8461–8469..
- , —, and E. A. Terray, 1994: Bottom boundary layer spectral dissipation estimates in the presence of wave motions. *Contin. Shelf Res.* **14**, 1239–1256..
- Guymner, I., and J. R. West, 1991: Field studies of the flow structure in a straight reach of the Conwy estuary. *Estuarine Coastal Shelf Sci.*, **32**, 581–596..
- Heathershaw, A. D., 1974: “Bursting” phenomena in the sea. *Nature*, **248**, 394–395..
- , 1979: The turbulent structure of the bottom boundary layer in a tidal current. *Geophys. J. Roy. Astrophys. Soc.*, **58**, 395–430..
- , and J. H. Simpson, 1978: The sampling variability of the Reynolds stress and its relation to boundary shear stress and drag coefficient measurements. *Estuarine Coastal Mar. Sci.*, **6**, 263–274..
- Hogstrom, U., 1988: Non-dimensional wind and temperature profiles in the atmospheric surface layer: A re-evaluation. *Bound.-Layer Meteor.*, **42**, 55–78..
- Huntley, D. A., 1988: A modified inertial dissipation method for estimating seabed stresses at low Reynolds numbers, with application to wave-current boundary layer measurements. *J. Phys. Oceanogr.*, **18**, 339–346.. [Find this article online](#)
- , and D. G. Hazen, 1988: Seabed stresses in combined wave and steady flow conditions on the Nova Scotia continental shelf: Field measurements and predictions. *J. Phys. Oceanogr.*, **18**, 347–362.. [Find this article online](#)
- Kaimal, J. C., J. C. Wyngaard, and D. A. Haugen, 1968: Deriving power spectra from a three-component sonic anemometer. *J. Appl. Meteor.*, **7**, 827–837.. [Find this article online](#)
- , I. Izumi, and O. R. Cote, 1972: Spectral characteristics of surface layer turbulence. *Quart. J. Roy. Meteor. Soc.*, **98**, 563–589..
- Limeburner, R., 1985: CODE-2: Moored array and large-scale data report. Tech. Rep. WHOI-85-35, Woods Hole Oceanographic Institution, Woods Hole, MA, 234 pp. [Available from Woods Hole Oceanographic Institute, Woods Hole MA 02543.].
- McLean, S. R., and J. D. Smith, 1979: Turbulence measurements in the boundary layer over a sand wave field. *J. Geophys. Res.*, **84**, 7791–7808..
- Mellor, G. L., and T. Yamada, 1974: A hierarchy of turbulence closure models for planetary boundary layers. *J. Atmos. Sci.*, **31**, 1791–1806.. [Find this article online](#)
- , and —, 1982: Development of a turbulence closure model for geophysical fluid problems. *Rev. Geophys. Space Phys.*, **20**, 851–875..
- Monin, A. S., and A. M. Yaglom, 1971: *Statistical Fluid Mechanics*. The MIT Press, 769 pp..
- Nunes, R. A., and J. H. Simpson, 1985: Axial convergence in a well-mixed estuary. *Estuarine Coastal Shelf Sci.*, **20**, 637–649..
- Phillips, O. M., 1980: *The Dynamics of the Upper Ocean*. Cambridge University Press, 336 pp..
- Pritchard, D. W., 1956: The dynamic structure of a coastal plain estuary. *J. Mar. Res.*, **15**, 33–42..
- Schlichting, H., 1979: *Boundary Layer Theory*. McGraw-Hill, 817 pp..

Smith, J. D., and S. R. McLean, 1977: Spatially averaged flow over a wavy surface. *J. Geophys. Res.*, **82**, 1735–1746..

Smith, R., 1976: Longitudinal dispersion of a buoyant contaminant in a shallow channel. *J. Fluid Mech.*, **78**, 677–688..

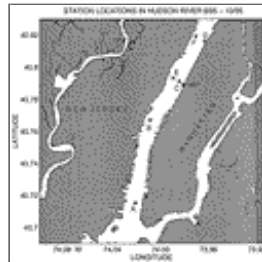
Soulsby, R. L., 1977: Similarity scaling of turbulence spectra in marine and atmospheric boundary layers. *J. Phys. Oceanogr.*, **7**, 934–937..
[Find this article online](#)

—, and K. R. Dyer, 1981: The form of the near-bed velocity profile in a tidally accelerating flow. *J. Geophys. Res.*, **86**, 8067–8074..

Tennekes, H., and J. L. Lumley, 1972: *A First Course in Turbulence*. The MIT Press, 300 pp..

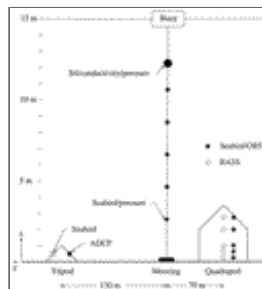
Williams, A. J., J. S. Tochko, R. L. Koehler, W. D. Grant, T. F. Gross, and C. V. R. Dunn, 1987: Measurement of turbulence in the oceanic bottom boundary layer with an acoustic current meter array. *J. Atmos. Oceanic Technol.*, **4**, 312–327..

Figures




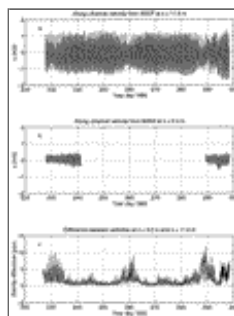
[Click on thumbnail for full-sized image.](#)

Fig. 1. Map of the study area.



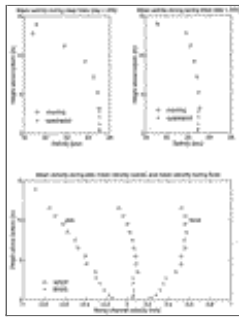
[Click on thumbnail for full-sized image.](#)

Fig. 2. Schematic diagram of instrumentation at site C, to approximate scale, looking along-channel to the north. Indicated in the diagram are the cross-channel (y) direction, positive toward New Jersey (see [Fig. 1](#) ) and the vertical (z) direction, positive upward.



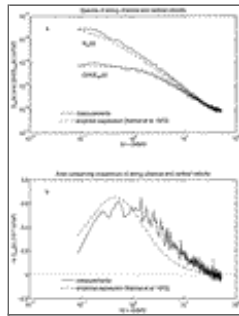
[Click on thumbnail for full-sized image.](#)

Fig. 3. Time series of (a) near-surface along-channel velocity, (b) near-bottom along-channel velocity, and (c) top-to-bottom salinity difference. The near-surface velocity measurements are from the ADCP bin 11.5 m above bottom. The near-bottom velocity measurements are from the BASS 1.18 m above bottom. The salinity differences are based on measurements obtained by Seabird sensors on the central mooring at depths of 4.3 and 12.3 m below the surface. The length of the near-bottom velocity records indicates the duration of the BASS deployments relative to the durations of the other fixed measurements. The coordinate system is defined so that positive velocities are in the direction of the flooding tide.



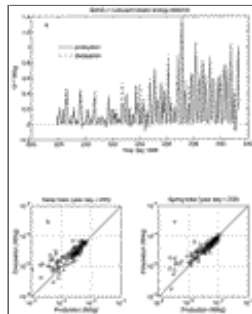
Click on thumbnail for full-sized image.

Fig. 4. Vertical structure, during BASS-1, of (a) mean salinity during neap tides, (b) mean salinity during spring tides, and (c) along-channel velocity. In panels (a) and (b) neap and spring refer to the first and second halves, respectively, of BASS-1. The bottom five salinity measurements were obtained by Seabird sensors on the BASS quadrapod and the remaining salinity measurements were obtained by Seabird sensors on the mooring at the central site. In panel (c), flood and ebb refer to periods when the depth-averaged velocity was positive and negative, respectively. The bottom five velocity measurements were from BASS and the remaining velocity measurements were obtained by the ADCP. In panel (b), the slightly unstable stratification indicated by the salinity measurements is not meaningful, because the uncertainty of the measurements is greater than the measured salinity differences.



Click on thumbnail for full-sized image.

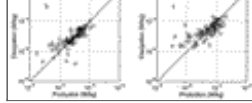
Fig. 5. Examples of (a) spectra and (b) cospectra of along-channel and vertical velocity, computed from measurements obtained by the BASS 1.18 m above bottom during BASS-1. The figures show averages of spectra obtained during all bursts when the burst-averaged along-channel velocity was in the flood direction and between 0.4 and 0.5 m s^{-1} . The dashed lines show empirical expressions presented by [Kaimal et al. \(1972\)](#) for the unstratified atmospheric surface layer. The empirical expressions have been modified to include spatial filtering, based on a line-average model of the acoustic travel-time BASS velocity sensors ([Kaimal et al. 1968](#)), aliasing, and a noise floor. The quantity $-u'w'$, required as input to the empirical expressions, was computed by integrating the averaged cospectrum in panel (b). In panel (a), the quantities $S_{uu}(k)$ and $(3/4)S_{ww}(k)$ should be equal in a truly isotropic inertial subrange ([Batchelor 1953](#)). $ka = 1$, where $a = 0.15 \text{ m}$ is the length of the BASS acoustic paths, corresponds to $kz \approx 8.0$ in this figure. The lowest resolved wavenumber in this figure is determined by the burst length, which was 3.28 min during BASS-1.



Click on thumbnail for full-sized image.

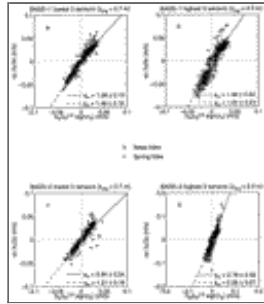
Fig. 6. BASS-1 estimates of production and dissipation in (a) time series form and in a direct comparison for (b) neap tides and (c) spring tides. The production and dissipation estimates are averages for the top two BASS, as explained in the text.





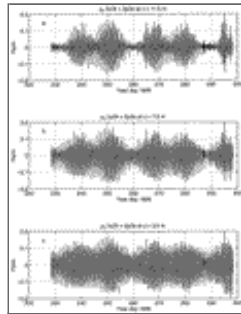
Click on thumbnail for full-sized image.

Fig. 7. BASS-2 estimates of production and dissipation in (a) time series form and in a direct comparison for (b) neap tides and (c) spring tides. The production and dissipation estimates are averages for the top two BASS, as explained in the text.



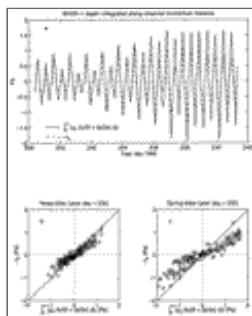
Click on thumbnail for full-sized image.

Fig. 8. Test of the law of the wall at two different heights and under different conditions. Estimates of $\kappa z \partial u / \partial z$ are based on regressions of u against $\log(z)$ for the bottom three BASS [panels (a) and (c)] and for the top three sensors [panels (b) and (d)], as explained in the text. The quantity z_{avg} is the average of the heights of the sensors involved in the regression. Positive τ_b corresponds to flooding tide. Error estimates for Φ_m correspond to 95% confidence intervals.



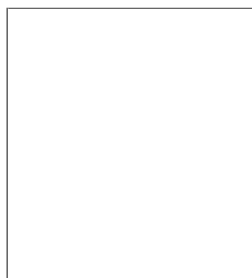
Click on thumbnail for full-sized image.

Fig. 9. Terms in a frictionless momentum balance at three heights above bottom.



Click on thumbnail for full-sized image.

Fig. 10. BASS-1 estimates of the terms in the along-channel momentum balance in (a) time series form and in a direct comparison for (b) neap tides and (c) spring tides. Values of bottom stress τ_b are based on direct covariance estimates of turbulent Reynolds shear stress, and values of $\partial p / \partial x$ are based primarily on differences between spatially separated measurements of bottom pressure, as explained in [section 2](#).



 Click on thumbnail for full-sized image.

Fig. 11. BASS-2 estimates of the terms in the along-channel momentum balance in (a) time series form and in a direct comparison for (b) neap tides and (c) spring tides. Values of bottom stress τ_b are based on direct covariance estimates of turbulent Reynolds shear stress, and values of $\partial p/\partial x$ are based primarily on differences between spatially separated measurements of bottom pressure, as explained in [section 2](#).



Click on thumbnail for full-sized image.

Fig. 12. Time series of amplitudes of terms in the depth-integrated along-channel momentum balance, computed as described in [section 3b](#).

Woods Hole Oceanographic Institution Contribution Number 9710.

Corresponding author address: Dr. John H. Trowbridge, Applied Ocean Physics and Engineering, Woods Hole Oceanographic Institution, Woods Hole, MA 02543.

E-mail: jtrowbridge@whoi.edu

[top](#) ▲



© 2008 American Meteorological Society [Privacy Policy and Disclaimer](#)
Headquarters: 45 Beacon Street Boston, MA 02108-3693
DC Office: 1120 G Street, NW, Suite 800 Washington DC, 20005-3826
amsinfo@ametsoc.org Phone: 617-227-2425 Fax: 617-742-8718
[Allen Press, Inc.](#) assists in the online publication of AMS journals.